Linking simple molecules to grain evolution across planet-forming disks

Salinas Poblete, V.N.

Citation

Salinas Poblete, V. N. (2017, December 18). *Linking simple molecules to grain evolution across planet-forming disks*. Retrieved from https://hdl.handle.net/1887/59500

Author: Salinas Poblete V.N.
Title: Linking simple molecules to grain evolution across planet-forming disks
Issue Date: 2017-12-18

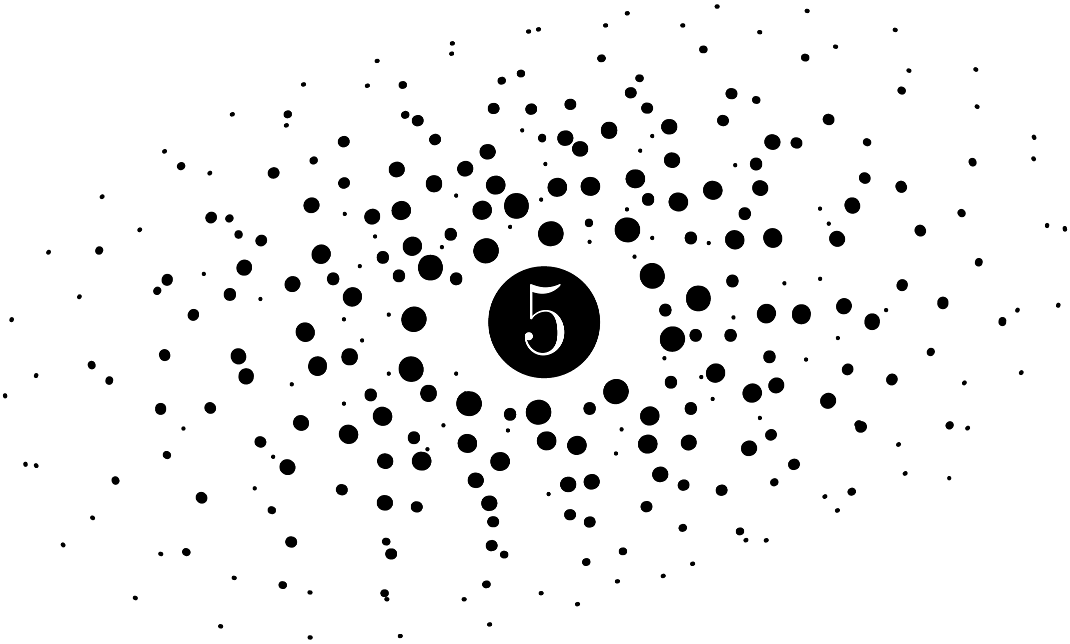

5

DCO$^+$, DCN, and N$_2$D$^+$ reveal three different deuteration regimes in the disk around the Herbig Ae star HD163296

Salinas, V. N., Hogerheijde, M. R., Mathews, G. S., Öberg, K. I., Qi, C., Williams, J. P., Wilner, D. J. 2017, A&A, 606, A125S.

5.1 Introduction

So far, more than 30 deuterated species have been detected toward prestellar cores and solar system bodies (Ceccarelli et al. 2007; Mumma & Charnley 2011). Their deuterium fractionation (D_f), usually higher than the D/H cosmic ratio of $\sim 10^{-5}$ (Vidal-Madjar 1991), is used to infer their thermal history, and in the case of solar system bodies, their location within the solar nebula at the time of formation. The amount of detections of deuterated species toward protoplanetary disks is not as high as in protostellar environments. DCO^+ has been detected in both T Tauri disks (Guilloteau et al. 2006; Öberg et al. 2010, 2011, 2015; van Dishoeck et al. 2003; Huang et al. 2017) and in the Herbig Ae disks HD163296 and MWC 480 (Qi et al. 2015; Mathews et al. 2013; Huang et al. 2017). DCN has been observed toward six different disks by Huang et al. (2017) and in addition DCN was previously observed toward TW Hya (Qi et al. 2008) and LkCa15 (Öberg et al. 2010). N_2D^+ has only been recently observed in the disk around the T Tauri star AS 209 (Huang & Öberg 2015).

The massive (0.089 $M_\odot$) and extended gas-rich disk around HD163296 is inclined at 44^o. Its proximity (122 pc) makes it an excellent laboratory to study the spatial location of the different deuteration regimes in protoplanetary disks (Qi et al. 2011; Mathews et al. 2013; Perryman et al. 1997). DCO^+ emission was first seen in a ring toward the disk around HD163296 and suggested as a tracer of the CO snowline by Mathews et al. (2013). It was later observed that the emission extended further inward past the CO snowline at 90 AU traced by N_2H^+ (Qi et al. 2015). Atacama Large Millimeter/submillimeter Array (ALMA) cycle 2 observations toward HD163296 of DCO^+, DCN, and N_2D^+ were presented by Yen et al. (2016) using a new stacking technique to enhance the signal to noise (S/N) of the radial profile confirming the extent of DCO^+. The observational study of Huang et al. (2017) found that both DCO^+ and $H^{13}CO^+$ show an emission break around 200 AU.

The ALMA continuum emission in Band 6 of HD163296 shows a rich structure of rings and depressions extending up to 230 AU (Isella et al. 2016; Zhang et al. 2016). This substructure could have an impact on the distribution and chemistry of certain species (See Sec. 5.5). The gas, traced by $C^{18}O$, extends out to 360 AU, well beyond the extent of the millimeter continuum emission, and scattered light has been detected up to ~500 AU (Garufi et al. 2014; Wisniewski et al. 2008). By contrasting the observations of key deuterated species to a physical model of HD163296, we hope to determine the origin of their formation and their relation to the location of the CO snowline. We carried out observations toward this disk using ALMA Band 6 and obtained spectral cubes of N_2D^+ (J=3–2), DCO^+ (J=3–2) and DCN (J=3–2).

The goal of this study is to constrain the radial location of these deuterated species in the disk surrounding the Herbig Ae star HD 163296 that trace different deuteration pathways. In Section 5.2 we present our data and their reduction. Section 5.3 shows the spatial characterization of the line emission. Section 5.4 contains our modeling approach and the derived parameters. Section 5.5 discusses the validity of our models and an interpretation of our observed molecules as a tracer for different deuteration pathways and their relation to the CO snowline. Finally, in Section 5.6 we give our conclusions.

5.2 Observations

We carried out observations of the disk surrounding the Herbig Ae star HD163296 (α_{2000} = $17^h56^m51\overset{s}{.}21$, δ_{2000} = $-21°57'22\overset{''}{.}0$) using ALMA in Band 6 as a part of Cycle 2 on the 27, 28, and 29 July 2014 (project 2013.1.01268.S). The total integration time on source was 4 hours and 43 min with thirty-three 12 m antennas. The correlator set up had seven

Table 5.1: Summary of our line observations.

Line transition	Frequency (GHz)	Integrated Intensity (mJy km s^{-1})	Beam	Channel rms (mJy/beam)
DCO$^+$ J=3–2	216.112	1270.45± 5.8	0.″53× 0.″42	3.25
DCN J=3–2	217.238	104.4± 5.6	0.″53×0.″42	3.11
N$_2$D$^+$ J= 3–2	231.321	61.6± 7.5	0.″50×0.″39	3.37

Notes. Line parameters of CLEAN images using natural weighting. The velocity integrated fluxes and their respective errors are calculated with a Keplerian mask as explained in Appendix 5.A.

different spectral windows (SPW); three of these contain H$_2$CO lines (Carney et al. 2017) while 3 others are centered on the rest frequencies of DCO$^+$ (J=3–2), N$_2$D$^+$ (J=3–2) and DCN (J=3–2), all of which have a resolution of 61 kHz. A final SPW contains wideband (2 GHz) continuum centered at 232.989 GHz. The quasar J1733-1304 was used as gain, bandpass, and total flux calibrator with 1.329 Jy on the lower sideband and 1.255 Jy in the upper sideband.

The data were calibrated following the standard CASA reduction as provided in the calibration scripts by ALMA. Baselines in the antenna array configuration correspond to a range in uv-distance of 20–630 kλ, which translates into a beam of ∼ 0.″33. Self-calibration was applied to the data as implemented by Carney et al. (2017). The DCO$^+$ (J=3–2), N$_2$D$^+$ (J=3–2) and DCN (J=3–2) lines were continuum subtracted in the visibility plane using a linear fit to the line-free channels and imaged by the CLEAN task in CASA. Figure 5.1 shows the integrated intensity maps of each line with and without a Keplerian mask. This mask is constructed by calculating the projected Keplerian velocities of the disk and matching them with the expected Doppler shifted emission in the spectral cube of the data (see Appendix 5.A). The N$_2$D$^+$ (J=3–2) emission is sitting on the edge of a strong atmospheric feature at high $T_{\rm sys}$. We fit the continuum only using the least noisy line-free channels from one side of the spectra (channels 350–750) but continuum subtraction is less accurate here.

5.3 Results

5.3.1 Detections

We successfully detected all of our target emission lines. Table 5.1 shows a summary of the line emission based on integrated intensity maps with Keplerian masking (lower panels of Fig.5.1).

Figure 5.2 shows the double -peaked spectra of DCO$^+$ (J=3–2), DCN (J=3–2) and N$_2$D$^+$ (J=3–2) at peak fluxes of 294 mJy, 48 mJy, and 54 mJy (without binning) corresponding to detections of 11σ, 5σ, and 4σ respectively. These spectra correspond to an aperture in the sky equal to the 1σ contour of DCO$^+$ in Fig. 5.1 for all lines. A simple Gaussian fit of the DCO$^+$ line profile gives a full width at half maximum (FWHM) of ~6.0 km s^{-1} and +5.8 km s^{-1} offset or systemic velocity consistent with values in the literature.

From the integrated intensity maps, shown in Fig. 5.1, N$_2$D$^+$ seems to be emitting from a broad ring with its peak flux at 9.3 mJy beam^{-1} km s^{-1} and a velocity integrated line intensity of 61.6± 7.5 mJy km s^{-1}. On the other hand, DCN emission is more compact, arising from within the N$_2$D$^+$ ring. As already noted by Huang et al. (2017) in their observations, we do not see clear evidence for an offset from the center as reported by Yen et al.

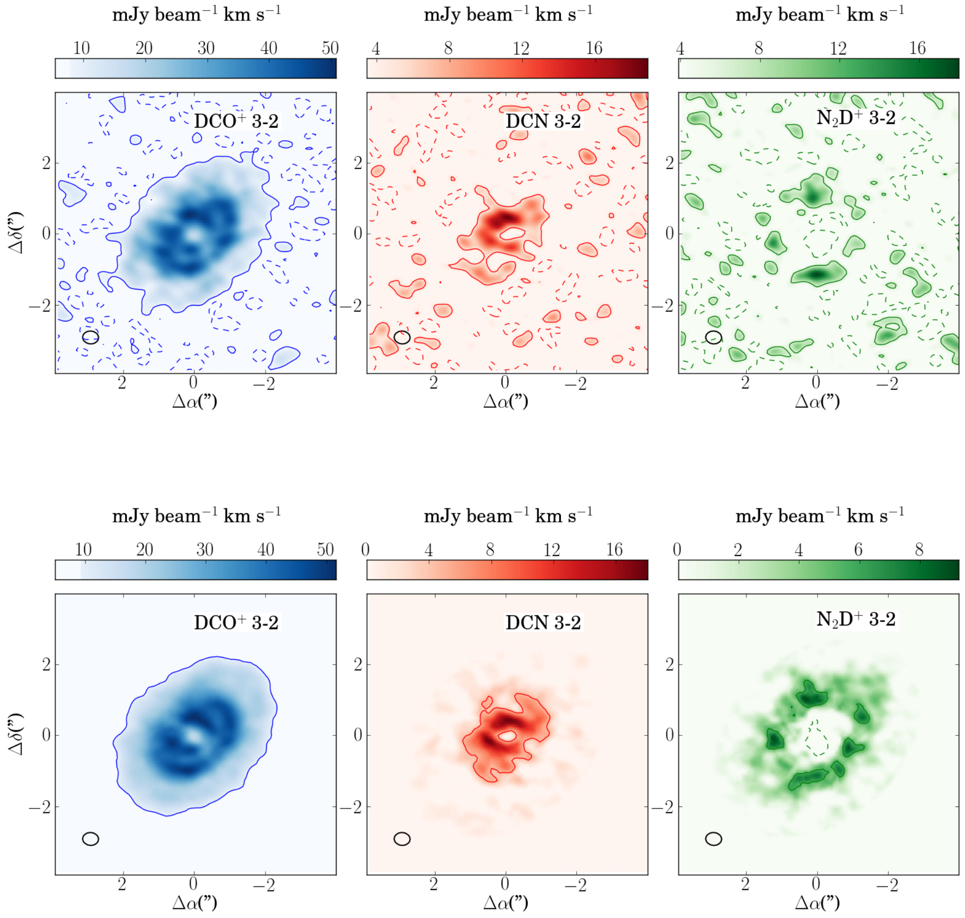

Figure 5.1: Integrated intensity maps of DCO$^+$, N$_2$D$^+$, and DCN with (lower panels) and without (upper panels) a Keplerian mask as explained in Appendix 5.A. The resulting synthesized beams of $0\farcs53\times0\farcs42$ for DCO$^+$ and DCN, and $0\farcs50\times0\farcs39$ for N$_2$D$^+$, with a beam position angle of 90^o, using natural weighting are shown at the lower left of each map. Contours are 1σ levels, where σ is estimated as the rms of an emission free region in the sky.

(2016). The emission peak is somewhat shifted northeast from what is observed by Huang et al. (2017). The total DCN velocity integrated line intensity is 104.4± 5.6 mJy km s^{-1} and the peak flux of its integrated intensity map is at 17.3 mJy beam^{-1} km s^{-1}. DCO$^+$ extends radially further inward than what was observed by Mathews et al. (2013) as confirmed by Qi et al. (2015) and Huang et al. (2017) within both of the N$_2$D$^+$ and N$_2$H$^+$ emission rings. The DCO$^+$ emission peaks at 51.5 mJy beam^{-1} km s^{-1} northwest, as noted by both Yen et al. (2016) and Huang et al. (2017), and has a velocity integrated line intensity of 1270.5± 5.8 mJy km s^{-1}.

Figure 5.3 shows the average radial profile of the integrated intensity maps of Fig. 5.1. This profile is constructed taking the average value of concentric ellipsoid annuli and their error is taken from the standard deviation. The projected linear resolution is lower along

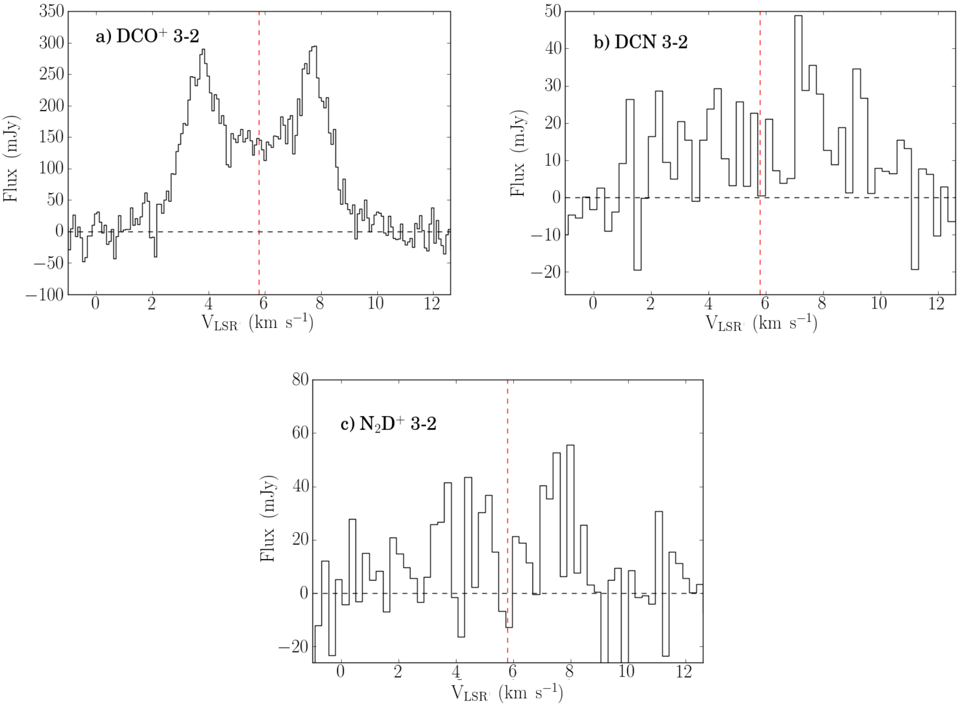

Figure 5.2: Spectra of a) DCO$^+$ J=3–2, b) DCN J=3–2 , and c) N$_2$D$^+$ J= 3–2 of the disk integrated values using a Keplerian mask as shown in Fig. 5.1. The DCN and N$_2$D$^+$ spectra have been binned to 3 times their resolution, 0.255 km/s and 0.238 km/s, respectively, to enhance their S/N ratio.

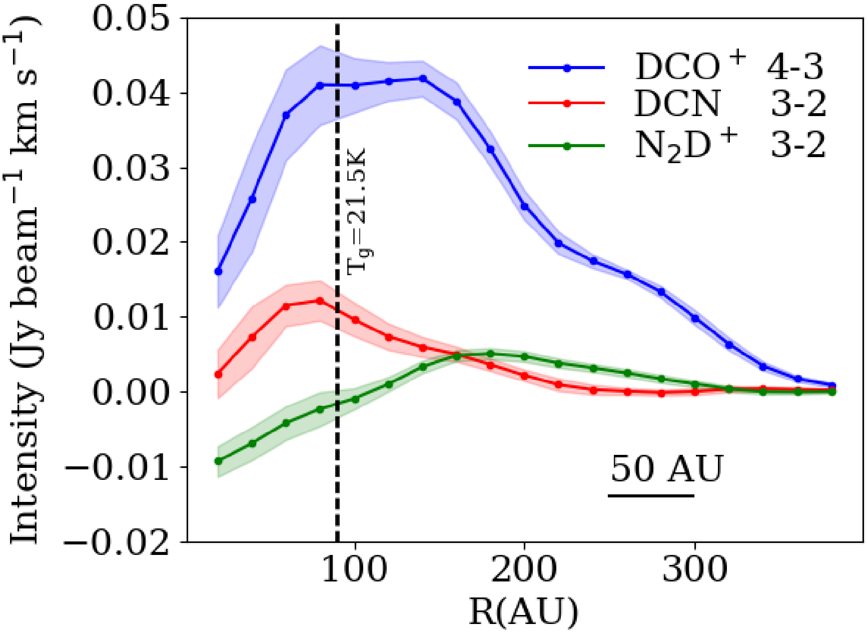

Figure 5.3: Radial profiles of the integrated intensity maps shown in Fig. 5.1. The shadowed color area represents the 3σ errors, where σ is the standard deviation in one elliptical annulus. The black dashed line corresponds to the location of the CO snowline (90 AU; Qi et al. 2015).

the semiminor axis than along the semimajor axis and therefore the resulting spatial resolution of the radial profiles is poorer than the synthesized beam. The N_2D^+ and DCN emission peak at ~160 AU and ~60 AU, respectively. The DCO$^+$ emission shows three peaks at 60 AU, 130 AU, and 250 AU, and extends up to 330 AU. Both the DCN and the DCO$^+$ radial profiles show a depression toward the center of the disk that is discussed in Sec. 5.5.

5.3.2 Column densities and deuterium fractionation

We can get an estimate of the disk-averaged column densities of the observed species if we consider the analytical formula from Remijan et al. (2003) for optically thin emission,

$$N = \frac{2.04 \int \Delta I dv}{\theta_a \theta_b} \frac{Q_{\rm rot} \exp(\frac{E_u}{T_{ex}})}{\nu^3 \langle S_{\rm ij} \mu^2 \rangle} \times 10^{20} \rm{cm}^{-2}, \tag{5.1}$$

where θ_a and θ_b (arcsec) corresponds to the semimajor and semiminor axes of the synthesized beam, $\int \Delta I dv$ is the total line flux (Jy beam^{-1} km s^{-1}), and T_{ex} (K) is the excitation temperature. The partition function (Q_{rot}), upper energy level (E_u K), line strength (S_{ij}), and dipole moment (μ Debye) were taken from the CDMS database.

We adopt two different disk-averaged excitation temperatures for each of the molecules: 10 and 25 K for N_2D^+ and 25 and 80 K for DCN and DCO$^+$. N_2D^+ should be abundant at temperatures $\lesssim$ 25 K where CO is frozen out (Qi et al. 2015) and at temperatures $\gtrsim$ 10 K where the low deuteration channel starts to be active. On the other hand, DCN and DCO$^+$

Table 5.2: Column density estimates for different excitation temperatures.

T_{ex}	N_{DCO^+} (cm^{-2})	N_{DCN} (cm^{-2})	$N_{N_2D^+}$ (cm^{-2})
10 K	-	-	$2.5 \pm 0.3 \times 10^{11}$
25 K	$1.68 \pm 0.01 \times 10^{12}$	$2.9 \pm 0.2 \times 10^{11}$	$1.6 \pm 0.2 \times 10^{11}$
80 K	$2.56 \pm 0.01 \times 10^{12}$	$5.2 \pm 0.3 \times 10^{11}$	-

Table 5.3: Deuterium fractionation estimates for different excitation temperatures.

T_{ex}	DCO^+/HCO^+	DCN/HCN	N_2D^+/N_2H^+
10 K	-	-	0.34±0.15
25 K	0.05±0.01	0.02±0.01	0.45±0.21
80 K	0.06±0.01	0.02±0.01	–

start to be abundant at higher temperatures where the high temperature pathway starts to be active (80K; see below Sec. 5.4.1). Table 5.2 summarizes our column density estimates for the three deuterated species using the values of the velocity integrated line intensities from Table 5.1. In general, our estimates do not differ by more than a factor of 2 within the excitation temperature ranges. Table 5.3 shows estimated disk-averaged D_f values for each of our species using the disk-averaged column densities from Table 5.2. We take the velocity integrated flux values of past line detections of $H^{13}CO^+$ J=3–2 (620 mJy beam^{-1} km s^{-1}), $H^{13}CN$ J=3–2 (170 mJy beam^{-1} km s^{-1}) (Huang et al. 2017), N_2H^+ J=3–2 (520 mJy beam^{-1} km s^{-1}) (Qi et al. 2015), and Eq. 5.1 to derive disk-average column densities assuming a $^{12}C/^{13}C$ ratio of 69 (Wilson 1999). The $^{12}C/^{13}C$ ratio can vary in disks between different C-bearing species (Woods & Willacy 2009). Higher or lower $^{12}C/^{13}C$ ratios for these species change D_f linearly. These D_f values are only lower limits as the species might not be spatially colocated.

5.4 Parametric modeling

5.4.1 Deuterium chemistry

The D/H ratio is specially useful to constrain the physical conditions of protoplanetary disks since an enhancement in this ratio is a direct consequence of the energy barrier of the reactions that deuterate simple molecules. We can distinguish the following three different key reactions that introduce deuterium into the most abundant species in protoplanetary disks (Gerner et al. 2015; Turner 2001):

$$H_3^+ + HD \leftrightharpoons H_2D^+ + H_2 + 230K, \tag{5.2a}$$

$$CH_3^+ + HD \leftrightharpoons CH_2D^+ + H_2 + 370K, \tag{5.2b}$$

$$C_2H_2^+ + HD \leftrightharpoons C_2HD^+ + H_2 + 550K. \tag{5.2c}$$

The right-to-left reaction of Equation 5.2a is endothermic and strongly enhances the D/H ratio of H_2D^+, and species that derive from it, in temperatures ranging from 10-30

K (Millar et al. 1989; Albertsson et al. 2013). This regime corresponds to the so-called low temperature deuteration channel. In contrast, the right-to-left reactions of Eq. 5.2b and 5.2c, involving light hydrocarbons, effectively enhance the deuterium fractionation in warmer temperatures ranging from 10-80 K. This regime corresponds to the high temperature deuteration channel.

N_2D^+ forms mainly through the low temperature deuteration channel via ion-molecule reaction (Dalgarno & Lepp 1984),

$$H_2D^+ + N_2 \longrightarrow N_2D^+ + H_2. \tag{5.3}$$

Hence the formation of N_2D^+ is expected to be enhanced at the same temperature range as H_2D^+.

DCN is formed out of two main reactions involving the low and high temperature channels with the latter being dominant (66%) (Turner 2001; Albertsson et al. 2013). Early works identify the low temperature channel as the key gas-phase formation of DCO^+ (Watson 1976; Wootten 1987). This pathway starts from Eq. 5.2a followed by the reaction

$$H_2D^+ + CO \longrightarrow DCO^+ + H_2. \tag{5.4}$$

However, recently modeling efforts by Favre et al. (2015) show that the high temperature channel may be an active formation pathway. If we consider Eq. 5.2b, DCO^+ can be formed via

$$CH_2D^+ + O \longrightarrow DCO^+ + H_2. \tag{5.5}$$

5.4.2 Motivation

Past observations of DCN in protoplanetary disks show centrally peaked distributions (Qi et al. 2008; Huang et al. 2017). This supports the idea that DCN is mainly formed through the high temperature deuteration pathway. If N_2D^+ and DCN are tracing the low and high temperature deuteration pathways, respectively, we can think of the DCO^+ emission as a linear combination of DCN and N_2D^+. Figure 5.4 shows, as an illustration, the DCO^+ radial profile subtracted first by the DCN emission scaled by a factor of 3.7 and then by the N_2D^+ emission scaled by a factor of 4.9. These factors can be interpreted as the ratio of their abundances. The first ring at 115 AU in the residuals, after subtracting both the DCN and N_2D^+ radial profile, can be interpreted as DCO^+ that is formed inside the CO snowline. If N_2D^+ is formed exclusively outside the snowline, its emission peak is shifted slightly outward (van't Hoff et al. 2017; Zhang et al. 2017) and its subtraction reveals DCO^+ formed by the low temperature channel in the regions in which CO is still present in the gas phase. The second residual ring at 280 AU indicates a third regime in which DCO^+ is present in the gas phase that does not correlate with the deuteration pathways regimes probed by DCN and N_2D^+. This analysis assumes that the line emission is optically thin and that it arises from the same disk region for the warm and cold channels.

We intend to characterize the three different regimes described above via a reasonable physical model for the disk and simple models for the column density of our species. In the following section we describe the adopted physical model and parametric abundances for N_2D^+, DCN, and DCO^+ that are used to fit the data.

5.4.3 Physical model

We adopted the physical model used by Mathews et al. (2013). This model was constructed by approximating the semi-parametric modeling of Qi et al. (2011) fitting the SED and the extent of their mm observations. The density structure is defined by

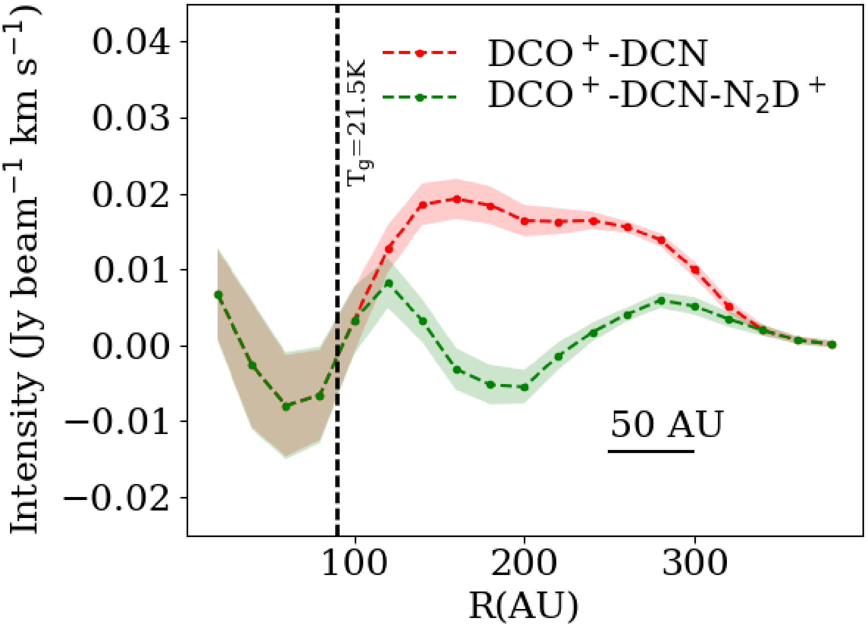

Figure 5.4: Residuals of the DCO$^+$ radial profile (as shown in Fig. 5.3) by subtracting first the DCN radial profile and then the N_2D^+ radial profile. The shadowed color area represents 1σ errors, where σ is the standard deviation in one elliptical annulus. The black dashed line corresponds to the location of the CO snowline (90 AU).

$$\Sigma_d(R) = \begin{cases} \Sigma_C \left(\frac{R}{R_c}\right)^{-1} \exp\left[-\left(\frac{R}{R_c}\right)\right] & \text{if } R \geq R_{\rm rim} \\ 0 & \text{if } R < R_{\rm rim,} \end{cases}$$

where $\Sigma_{\rm C}$ is determined by the total disk mass $M_{\rm disk}$ (0.089 $M_\odot$ using a gas-to-dust ratio of 0.0065), $R_{\rm C}$ (150 AU) is the characteristic radius, and $R_{\rm rim}$ (0.6 AU) is the inner rim of the disk. The vertical structure is treated as a Gaussian distribution with an angular scale height defined by

$$h(R) = h_{\rm C} \left(\frac{R}{R_{\rm C}}\right)^{\psi},$$

where ψ (0.066) is the flaring power of the disk and $h_{\rm C}$ is the angular scale height at the characteristic radius $R_{\rm C}$. The parameter $h_{\rm C}$ takes different two values for the dust vertical distribution and two more for the gas vertical distribution. The parameters $h_{\rm small}$(0.08) and $h_{\rm large}$ (0.06) describe the distribution of small and large dust grains, respectively, while $h_{\rm main}$ (0.1) and $h_{\rm tail}$ (0.2) describe the main bulk distribution of gas in the mid-plane of the disk and the tail of gas that continues the upper regions of the disk surface (See appendix A of Mathews et al. 2013). The gas temperature profile was computed by the 2D radiative transfer code RADMC (Dullemond & Dominik 2004) assuming $T_{\rm gas} = T_{\rm dust}$. This code receives the stellar parameters as listed in Mathews et al. (2013) and the dust density distribution as inputs.

5.4.4 N_2D^+, DCN, and DCO^+ abundance models

DCN is formed mainly (66%) through deuterated light hydrocarbons such as CH_2D (see Fig. 5c of Turner 2001). This reaction starts with the deuteration of CH_3^+, the so-called high temperature deuteration pathway. For an enhancement of CH_2D^+ over CH_3^+ temperatures should not exceed ~10–80 K. We use a simple toy model for DCN taking the same approach as for the N_2D^+ model with three free parameters: an an inner radius $R_{\rm in}$ beyond which it is sufficiently cold for an enhancement of the CH_2D/CH_3^+ ratio, an outer radius $R_{\rm out}$, and a constant abundance $X_{\rm high}$.

N_2D^+ is formed by the reaction of N_2 with H_2D^+. We expected considerable abundances of N_2D^+ only outside the CO snowline because its parent molecule, H_3^+, is readily destroyed by the proton exchange with CO. This is also true for its non-deuterated form N_2H^+. We used a simple ring model to constrain the spatial distribution of gas N_2D^+. The model consists of three free parameters: an inner radius $R_{\rm in}$ beyond the CO snowline and where conditions are sufficiently cold for a substantial enhancement of the H_2D^+/H_3^+ ratio, an outer radius $R_{\rm out}$, and a constant abundance $X_{\rm low}$.

We modeled the distribution of DCO^+ as three separate contributions from both deuteration channels and a third region in the outer disk motivated by the radial profile of its integrated intensity map (Fig. 5.4). Our model uses a set of seven parameters describing three regions: an inner radius ($R_{\rm in}$), two radial breaks (R_1, R_2), and three constant abundances ($X_{\rm high}$, $X_{\rm low}$, X_3) for the inner, the middle and the outer emission region. Figure 5.5 shows abundances and column density profiles of these simple models.

5.4.5 Line excitation

Instead of a full radiative transfer modeling we opted for a more simplistic approach by considering estimates of a characteristic excitation temperature as a function of the distance to the central star to calculate the resulting line emission given an abundance profile. We used

LIME (Brinch & Hogerheijde 2010, v1.5), a 3D radiative transfer code in non-LTE that can produce line and continuum radiation from a physical model to estimate a characteristic excitation temperature as a function of radius throughout the disk for the observed transitions DCO$^+$ 3–2, DCN 3–2, and N$_2$D$^+$ 3–2. We used the physical model described above and a constant abundance equal to the disk average found in Sec. 5.3 assuming $T_{\rm ex}$ = 25 K. LIME outputs population levels in a grid of 50000 points, which are randomly distributed in R using a logarithmic scale. Establishing a convergence criteria encompassing all of the grid points is difficult. We manually set the number of iterations to 12 and confirm convergence by comparing consecutive iterations. We used the rate coefficients from the Leiden Atomic and Molecular Database (Schöier et al. 2005)[1]. For N$_2$D$^+$ and DCN we used the N$_2$H$^+$ rate coefficients, which are adopted from HCO$^+$ (Flower 1999), and HCN rate coefficients (Dumouchel et al. 2010), respectively, since the transitions between the non-deuterated and deuterated forms do not differ significantly. For DCO$^+$ we use the same collision rates as those for HCO$^+$ and Einstein A coefficients taken from the Cologne Database for Molecular Spectroscopy (CDMS) and Jet Propulsion Laboratory (JPL) database.

To construct the radial excitation temperature profile we take the average excitation temperature of the points below $z < 10\times h(R)$, where $h(R)$ is the scale height of our adopted physical model. These temperature profiles are shown in red in Fig. 5.5. A drawback of this approach is that assuming an isothermal vertical structure of the temperature profile might not properly describe the vertical region over which the molecules extend.

5.4.6 Abundance estimates

We computed a radial emission profile with the radial excitation temperature profile and column densities from the parametric constant abundance profiles, shown in green in Fig.5.5, by solving Eq.5.1.

We then created a 2D sky image from the modeled emission profile and convolved it with the synthesized beam of the observation to fit the integrated intensity maps shown in Fig. 5.1. Since we only fit radial column density profiles the vertical distribution of these species cannot be constrained by this approach. However, past modeling of DCO$^+$ shows that its vertical distribution has limited effect on constraining radial boundaries (Qi et al. 2015).

5.4.7 Best-fit parameters

We minimize $\chi^2 = (F_{\rm obs}(x,y) - F_{\rm model}(x,y))^2/\sigma(x,y)^2$ values, where $F_{\rm obs}(x,y)$ corresponds to the data points of the integrated intensity maps (as shown in Fig. 5.1), $F_{\rm model}(x,y)$ corresponds to the points of the modeled integrated intensity map convolved with the synthesized beam and $\sigma(x,y)$ corresponds to the standard deviation of the pixels of a concentric ellipsoid (such as those used to make the radial profiles seen in Fig.5.3) that includes the pixel (x,y). We report best-fit parameters that correspond to a minimum of the explored parameter space. In the case of DCO$^+$ we explore different configurations of rings, allowing them to have one, two or no gaps empty of material between the ring-like regions. Table 5.4 shows a summary of our preferred models and Fig. 5.6 shows radial profiles of the best-fit model's column density, integrated intensity, estimated excitation temperature, and the integrated intensity of the data for each of our detections.

In the case of DCO$^+$, the location of the different radial zones are degenerate. A model with an additional two degrees of freedom, describing three radial rings separated by gaps,

---

[1] www.strw.leidenuniv.nl/~moldata/

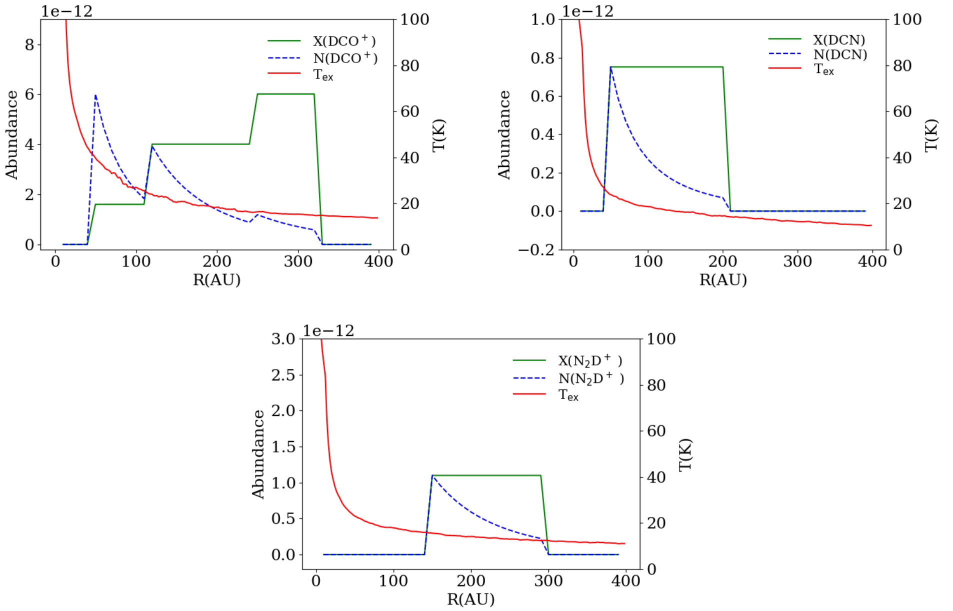

Figure 5.5: Schematics of the abundance models for the transitions of DCO$^+$ J=3–2, DCN J=3–2 and N$_2$D$^+$ J=3–2. The dashed blue line corresponds to a scaled profile of the column density of the abundance model for the purpose of illustration. The red continuous line corresponds to the assumed excitation temperature profile.

can also reproduce the data. The modest spatial resolution of our data cannot distinguish between these models. Detailed chemical modeling plus a 3D radiative treatment of DCO$^+$ is necessary to break the degeneracy of our toy model. The best-fit abundances for the simplest model without any gaps as described in Sec. 5.4.4 are $X_{\rm high}$=$1.6^{+0.4}_{-0.5}\times10^{-12}$, $X_{\rm low}$=$4.0^{+1.0}_{-1.3}\times10^{-12}$, X_3=$6.0^{+1.4}_{-2.0}\times10^{-12}$, and their best-fit radial boundaries are $R_{\rm in}$=50^{+5}_{-3} AU, R_1=118^{+4}_{-5} AU , R_2=245^{+3}_{-13} AU, and $R_{\rm out}$=316^{+3}_{-10} AU. We do not consider a vertical distribution of the DCO$^+$ and DCN molecules. This results in vertically averaged abundances, which are lower limits to the maximum values expected in a full 2D treatment because in reality DCO$^+$ and DCN are absent where the gas temperature is higher than the activation temperature for their deuteration. In addition, DCO$^+$ is absent in the midplane where CO starts to freeze-out.

The best-fit model for the DCN emission profile consists of a ring with a constant abundance $X_{\rm high}$=$7.5^{+0.9}_{-0.9}\times10^{-13}$ between $R_{\rm in}$=51^{+6}_{-6} AU and $R_{\rm out}$=201^{+15}_{-24} AU, where $R_{\rm in}$ can be considered the radius where the gas temperature is high enough for the reaction described in Eq. 5.2b to be exothermic. The best-fit model for the N$_2$D$^+$ emission profile consists of a ring with constant abundance $X_{\rm low}$=$1.1^{+0.1}_{-0.1}\times10^{-12}$ between $R_{\rm in}$=139^{+5}_{-4} AU and $R_{\rm out}$=287^{+15}_{-21} AU, where $R_{\rm in}$ could be tracing the CO midplane snowline radial location.

Table 5.4: Best-fit model parameters

Parameters	DCN J=3–2	N_2D^+ J= 3–2	DCO^+ J=3–2
R_{in}	51^{+6}_{-6} AU	139^{+5}_{-4} AU	50^{+5}_{-3} AU
R_1			118^{+4}_{-5} AU
R_2			245^{+3}_{-13} AU
R_{out}	201^{+15}_{-24} AU	287^{+15}_{-21} AU	316^{+3}_{-10} AU
X_{high}	$7.5^{+0.9}_{-0.9}\times10^{-13}$		$1.6^{+0.4}_{-0.5}\times10^{-12}$
X_{low}		$1.1^{+0.1}_{-0.1}\times10^{-12}$	$4.0^{+1.0}_{-1.3}\times10^{-12}$
X_3			$6.0^{+1.4}_{-2.0}\times10^{-12}$

Notes. Best-fit parameters of models as shown in Fig. 5.6. DCO^+ values correspond to the model with two gaps. The formal errors are calculated at 90% confidence levels.

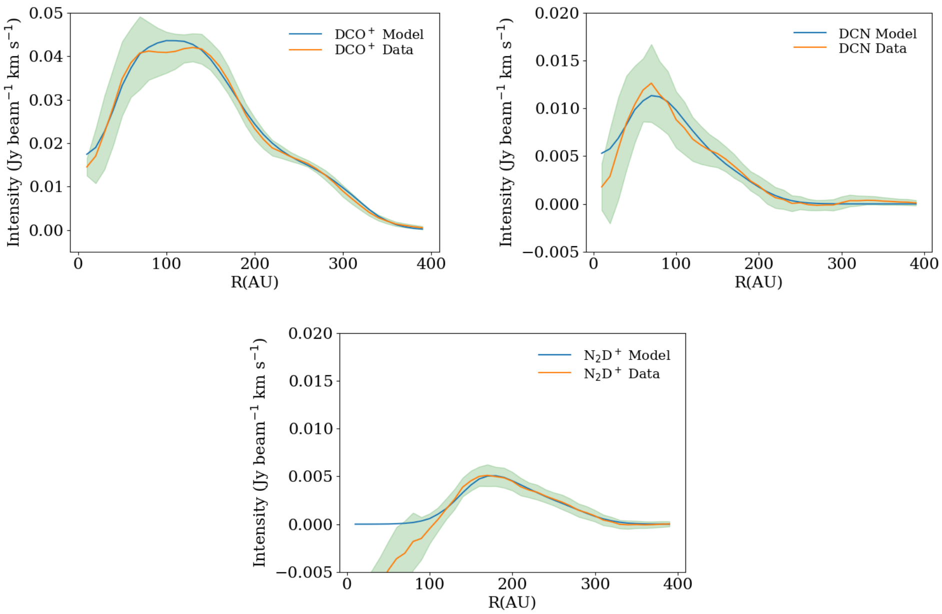

Figure 5.6: Best-fit models for the transitions of DCO^+ J=3–2, DCN J=3–2, and N_2D^+ J=3–2. The error bars, shown as a filled region in green, correspond to the standard deviation of the values in one annulus as seen in Fig. 5.3.

5.5 Discussion

5.5.1 The inner depression

Our best-fit models find an inner drop in emission at ~50 AU for both the DCN and DCO^+ line emission. This could be tracing the gas temperature required for the high temperature deuteration channel to be active (10-80 K) or an optically thick continuum region at small radii. Recent observations of $C^{18}O$, ^{13}CO, and continuum at 1.3 mm (Isella et al. 2016) with ALMA in higher spatial resolution also show a central depression in $C^{18}O$ and ^{13}CO radial intensity profiles. These CO isotopes are optically thin and trace the gas near the midplane. If the dust becomes optically thick it could hide the line emission coming from deeper layers toward the midplane. Subtracting the continuum estimate in these regions then creates an apparent absence of emission. An alternative explanation is inherent to the chemistry of both species. DCN is readily destroyed by simple ions such as H_3^+ and H^+ (Albertsson et al. 2013). DCO^+ can be destroyed if H_2O is desorbed from the grains at inner radii. It is unlikely that both of these effects correlate at the same radii (R_{in} ~50 AU).

The peak value of the continuum at the center of the disk is 167 mJy beam^{-1} corresponding to a brightness temperature of 25 K at 1.3 mm. This is inconsistent with the expected dust temperature derived from SED models for optically thick dust. The disk surrounding HD163296 is known to have unresolved ring-like structure at 1.3 mm (Zhang et al. 2016; Isella et al. 2016). The corresponding brightness temperature for the peak intensity in these observations at higher spatial resolution is 55 K, which is consistent with optically thick dust. The best-fit continuum models of Isella et al. (2016) show optically thick dust just inside 50 AU. We conclude that our R_{in} parameter is tracing this optically thick dust region.

5.5.2 Limitation of DCO^+ as a CO snowline tracer

N_2H^+ has been used to trace the CO snowline in protoplanetary disks before (Qi et al. 2015, 2013). We expect N_2D^+ to trace it as well using the same reasoning as for N_2H^+ (Huang & Öberg 2015). Our best-fit N_2D^+ model gives a R_{in} value of 141 AU, which is 50 AU further away than previous estimates of the CO snowline in HD 163296. This could be due to the apparent central depression in the N_2D^+ radial profile. As explained in Sec. 5.2, this line is sitting on the edge of an atmospheric feature resulting in high noise and a very weak detection, which makes it difficult to do a good continuum subtraction. The central negative bowl has the same order of magnitude as other scattered negative noise in the image plane of the resulting integrated intensity map, but, as it is located at the center, an azimuthal average does not represent as good an estimate of the radial profile in the inner disk as it does in the outer disk. We cannot rely on our best-fit value for R_{in} as a probe for the CO snowline in the midplane, although a deeper integration of the N_2D^+ J=3–2 line can still be used to constrain it.

On the other hand, our best-fit DCO^+ model value for R_1 of 118^{+4}_{-5} AU agrees well with the previous estimate of ~90 AU given our resolution. Two effects are boosting the deuterium fractionation of H_2D^+ and, in consequence, the low temperature deuteration channel. First, the gas temperature is low enough for the reaction in Eq. 5.2a to be mainly exothermic. Second, H_2D^+ is readily destroyed by CO in the gas phase which is frozen out. But CO must be present to form DCO^+ via Eq. 5.5. This could be achieved in a scenario in which DCO^+ is found in a thin layer around the CO freeze-out temperature as proposed by Mathews et al. (2013). Without previous knowledge, DCO^+ alone cannot trace the location of the CO snowline.

5.5.3 The origin of the third ring

Motivated by the reasoning in Section 5.4.2 we found a best-fit value of 245^{+3}_{-13} AU for the R_2 parameter in our DCO$^+$ model. At these radii the bulk of CO in the gas phase is locked up on the grains as ice. The main production route of DCO$^+$ in the low temperature deuteration route (Eq.5.4) requires CO in the gas-phase. This raises the question of how DCO$^+$ emission arises at such large radii.

Photodesorption of CO by nonthermal processes could explain an outer ring of DCO$^+$ emission as discussed in the case of IM Lup (Öberg et al. 2015). However the efficiency of this mechanism is very model dependent. Full chemical models of DCO$^+$ toward DM Tau (Teague et al. 2015) show that, although there is an enhancement of DCO$^+$ at large radii produced by the interstellar UV field and X-ray luminosity, the effect is not as pronounced as that seen in IM Lup. The strongly emitting outer disk seen toward IM Lup coincides with the extent of the mm-size grains. If the smaller grains also follow the steepening of the surface density of mm-size grains, UV penetration is enhanced leading to an enhancement on the DCO$^+$ emission. High-resolution continuum data observed with ALMA Band 6 (Isella et al. 2016) revealed three concentric sets of rings and gaps as predicted by Zhang et al. (2016). The first depression at $D_1 \sim 53$ AU and the second brightness peak centered at $B_2 \sim 120$ AU correlate well with $R_{\rm in}=50^{+5}_{-3}$ AU and $R_1=118^{+4}_{-5}$ AU from our best-fit DCO$^+$ model. The extent of the continuum to about 230 AU also correlates with R_2 at 245^{+3}_{-13} AU from our best-fit DCO$^+$ model. Although no direct consequence of the location of the second gap can be drawn toward an enhancement in UV penetration, the scales at which these rings are seen in the (sub)mm continuum (~ 60-50 AU) are a rough estimate of the spatial scales where rings and gaps are seen in shorter wavelengths. Full grain-surface chemical modeling is needed to identify the chemical reactions involved in this mechanism.

Cleeves (2016) have proposed a thermal inversion in the midplane as a mechanism to release CO into the gas phase at large radii. Recently, dust evolution modeling efforts by Facchini et al. (2017), coupled with chemistry models of HD 163296, shows signs of thermal inversion as a direct consequence of radial drift, grain growth, and settling. As a result, thermal CO desorption is enhanced at large radii where the dust becomes warmer. The thermal inversion in the models of Facchini et al. (2017) occurs at about 400 AU, farther away than our R_2 best-fit parameter of 245^{+3}_{-13} AU. However, the radial location of the thermal inversion is very temperature sensitive and a slightly colder disk could shift its location inward. This effect is only seen in models with a low turbulence α of 10^{-3}-10^{-4} and when the CO ice is mixed with water ice resulting in a higher binding energy. A tailored model is necessary to confirm the viability of this mechanism as an explanation for the outer DCO$^+$ ring.

Finally, another plausible explanation is a local decrease of the ortho- to para- (o/p) ratio of H_2. The reaction shown in Eq.5.2a has a higher activation barrier for p-H_2 than for o-H_2 which results in an increase in DCO$^+$ formation (Murillo et al. 2015; Walmsley et al. 2004). Detailed chemical modeling is needed to test this scenario.

5.5.4 Deuterium fractionation

Our estimated disk-averaged fractionation ratio D_f(DCO$^+$/HCO$^+$) of 0.05±0.01 agrees with previous measurements on this source (Huang et al. 2017) or even toward other disks, for example, DM Tau (Guilloteau et al. 2006) and TW Hya (van Dishoeck et al. 2003).

Our estimated value of 0.02±0.01 for D_f(DCN/HCN) is lower than the D_f(DCO$^+$/HCO$^+$) and D_f(N_2D^+/N_2H^+). A lower value of D_f(DCN/HCN) compared to D_f(N_2D^+/N_2H^+) could hint at a more efficient deuterium enrichment in the outer colder disk. On the other hand, in comparison with $D_f(DCO^+/HCO^+)$, a lower value of $D_f(DCN/HCN)$ could be explained by the different deuteration pathways that formed these species, supporting the idea of a colder formation environment for DCO^+ at large radii. Both of these values are of the same order of magnitude as for other protoplanetary disks (Öberg et al. 2012; Huang et al. 2017). The derived $D_f(DCO^+/HCO^+)$ value is one order of magnitude lower than in starless cores but similar to the value toward low-mass protostars, such as IRAS 16293-2422 (Butner et al. 1995; Caselli et al. 2002; Tafalla et al. 2006; Schöier et al. 2002). The derived $D_f(DCN/HCN)$ value is the same order of magnitude toward low-mass protostars and starless cores (Wootten 1987; Roberts et al. 2002).

Our estimated value of 0.45±0.21 for $D_f(N_2D^+/N_2H^+)$ is higher than $D_f(DCO^+/HCO^+)$ and $D_f(DCO^+/HCO^+)$ as predicted by the chemical models of Willacy (2007). It is also comparable to the values toward the T Tauri disk AS 209 (Huang & Öberg 2015) and consistent with the wide range of ratios, from <0.02 to 0.44, found toward starless cores (Crapsi et al. 2005). As noted in the case of AS 209, the higher D/H ratio from N_2D^+ compared to that from DCO^+ is a consequence of their formation environments. DCO^+ is formed where CO is not frozen out in the relatively warm upper layers of the disk. N_2D^+ is more abundant where CO is frozen out and deuteration is enhanced by Eq. 5.2a which, together with N_2H^+, makes it an excellent tracer of the cold outer midplane.

5.6 Summary

We have successfully detected three deuterated species toward HD 163296: DCO^+, N_2D^+, and DCN. We use simple models and estimates of the midplane temperature to fit radial rings with constant abundance constraining their relative abundance and radial location. Our main conclusions are:

- We confirm the location of the CO snowline using the second ring of DCO^+ as a tracer at ~100 AU, which is consistent with the previously reported value of 90 AU. Our N_2D^+ detection is too noisy to effectively constrain its location, although it is still consistent given our large beam.

- DCO^+ and DCN show an inner depression that arises most likely due to optically thick dust and not due to inherent formation pathway of both species.

- DCO^+ shows a three ring-like structure, located at 70 AU, 150 AU, and 260 AU that could be linked to the structure of the μm-sized grains. The two first rings correspond to the high and low temperature deuteration pathways and are in agreement with simple DCN and N_2D^+ best-fit models.

- The origin of the third DCO^+ ring at 260 AU may be due to a local decrease of UV opacity allowing the photodesorption of CO and consequent formation of DCO^+ as seen in other disks (Öberg et al. 2015), thermal desorption of CO as proposed by Facchini et al. (2017), or a local decrease of the o/p ratio of H_2.

- The derived D_f values are several orders of magnitude higher than the D/H cosmic ratio as expected and are in agreement with previous measurements and models. The higher D/H value for N_2D^+ in comparison with those from DCO^+ and DCN suggest a cooler formation environment for the former.

  Detailed chemical modeling of these molecules is needed to confirm the origin of the DCO^+ rings.

Acknowledgements. The authors acknowledge support by Allegro, the European ALMA Regional Center node in The Netherlands, and expert advice from Luke Maud in particular. This work was partially supported by grants from the Netherlands Organization for Scientific Research (NWO) and the Netherlands Research School for Astronomy (NOVA) This paper makes use of the following ALMA data: ADS/JAO.ALMA# 2013.1.01268.S. ALMA is a partnership of ESO (representing its member states), NSF (USA), and NINS (Japan), together with NRC (Canada), NSC and ASIAA (Taiwan), and KASI (Republic of Korea), in cooperation with the Republic of Chile. The Joint ALMA Observatory is operated by ESO, AUI/NRAO, and NAOJ.

5.A Keplerian Masking

Since the emission in each channel only comes from a region in the sky where the rotational velocity of the disk matches the Doppler shift of the line, selecting a subset of pixels on each velocity channel with Keplerian velocities equal to the expected Doppler shift enhances the S/N of the final integrated intensity map. To achieve this, we first calculate the projected radial velocity on each pixel using a stellar mass value of 2.3 $M_\odot$ (van den Ancker et al. 1997). We create a mask cube with the same dimensions as the data spectral cube and select, for each spectral plane, the pixels that have a projected radial velocity greater than the correspondent Doppler-shifted velocity v_r of the spectral plane and lower than $v_r + \delta v$, where δv is the spectral resolution of the cube. Finally, each spectral plane of the mask cube is convolved with the synthesized beam to create a final mask that accounts for the smearing of the disk as seen in Fig 5.7.

A similar approach has already been used by Yen et al. (2016), stacking azimuthal regions that are corrected by their Keplerian velocity. They reconstruct integrated intensity maps by Doppler-shifting a selected azimuthal region within an inner and outer radius. Since both methods are flux conserving, the only difference lies in reduced noise for the latter in sacrifice of spatial information. The stacking method by Yen et al. (2016) achieves a S/N increase of a factor of $\sim$ 4 for the weak lines N_2D^+ J=3–2 and DCN J=3–2. In contrast our method achieves an increase in S/N of a factor of $\sim$ 2 but results in a much clearer integrated intensity map (see Fig. 5.1).

Bibliography

Albertsson, T., Semenov, D. A., Vasyunin, A. I., Henning, T., & Herbst, E. 2013, ApJS, 207, 27
Brinch, C., & Hogerheijde, M. R. 2010, A&A, 523, A25
Butner, H. M., Lada, E. A., & Loren, R. B. 1995, ApJ, 448, 207
Carney, M. T., Hogerheijde, M. R., Loomis, R. A., et al. 2017, ArXiv e-prints, arXiv:1705.10188
Caselli, P., Walmsley, C. M., Zucconi, A., et al. 2002, ApJ, 565, 344
Ceccarelli, C., Caselli, P., Herbst, E., Tielens, A. G. G. M., & Caux, E. 2007, Protostars and Planets V, 47
Cleeves, L. I. 2016, ApJ, 816, L21
Crapsi, A., Caselli, P., Walmsley, C. M., et al. 2005, ApJ, 619, 379
Dalgarno, A., & Lepp, S. 1984, ApJ, 287, L47
Dullemond, C. P., & Dominik, C. 2004, A&A, 417, 159
Dumouchel, F., Faure, A., & Lique, F. 2010, MNRAS, 406, 2488
Facchini, S., Birnstiel, T., Bruderer, S., & van Dishoeck, E. F. 2017, ArXiv e-prints, arXiv:1705.06235
Favre, C., Bergin, E. A., Cleeves, L. I., et al. 2015, ApJ, 802, L23
Flower, D. R. 1999, MNRAS, 305, 651
Garufi, A., Quanz, S. P., Schmid, H. M., et al. 2014, A&A, 568, A40
Gerner, T., Shirley, Y. L., Beuther, H., et al. 2015, A&A, 579, A80
Guilloteau, S., Piétu, V., Dutrey, A., & Guélin, M. 2006, A&A, 448, L5

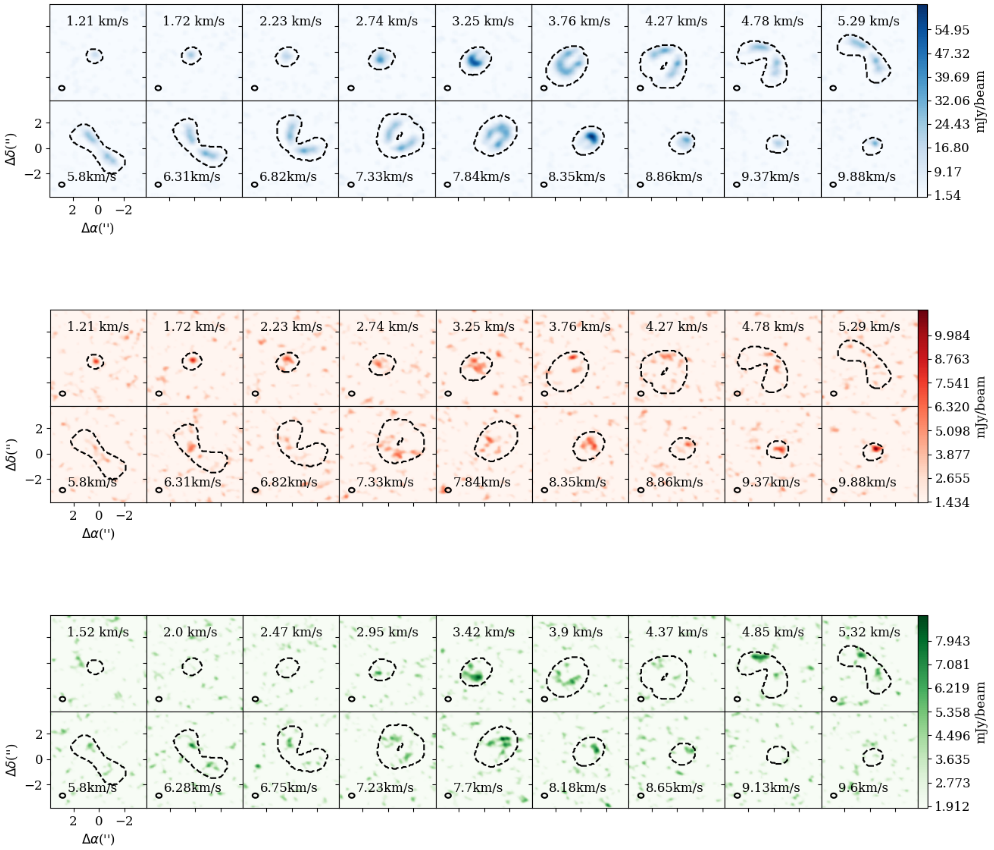

Figure 5.7: Overplotted Keplerian mask, in black dashed contours, and spectral maps of DCO$^+$ J=3–2, DCN J=3–2, and N$_2$D$^+$ J=3–2.

Huang, J., & Öberg, K. I. 2015, ApJ, 809, L26
Huang, J., Öberg, K. I., Qi, C., et al. 2017, ApJ, 835, 231
Isella, A., Guidi, G., Testi, L., et al. 2016, Phys. Rev. Lett., 117, 251101
Mathews, G. S., Klaassen, P. D., Juhász, A., et al. 2013, A&A, 557, A132
Millar, T. J., Bennett, A., & Herbst, E. 1989, ApJ, 340, 906
Mumma, M. J., & Charnley, S. B. 2011, ARA&A, 49, 471
Murillo, N. M., Bruderer, S., van Dishoeck, E. F., et al. 2015, A&A, 579, A114
Öberg, K. I., Boogert, A. C. A., Pontoppidan, K. M., et al. 2011, ApJ, 740, 109
Öberg, K. I., Furuya, K., Loomis, R., et al. 2015, ApJ, 810, 112
Öberg, K. I., Qi, C., Wilner, D. J., & Hogerheijde, M. R. 2012, ApJ, 749, 162
Öberg, K. I., Qi, C., Fogel, J. K. J., et al. 2010, ApJ, 720, 480
Perryman, M. A. C., Lindegren, L., Kovalevsky, J., et al. 1997, A&A, 323, L49
Qi, C., D'Alessio, P., Öberg, K. I., et al. 2011, ApJ, 740, 84
Qi, C., Öberg, K. I., Andrews, S. M., et al. 2015, ApJ, 813, 128
Qi, C., Wilner, D. J., Aikawa, Y., Blake, G. A., & Hogerheijde, M. R. 2008, ApJ, 681, 1396
Qi, C., Öberg, K. I., Wilner, D. J., et al. 2013, Science, 341, 630

Remijan, A., Snyder, L. E., Friedel, D. N., Liu, S.-Y., & Shah, R. Y. 2003, ApJ, 590, 314
Roberts, H., Fuller, G. A., Millar, T. J., Hatchell, J., & Buckle, J. V. 2002, A&A, 381, 1026
Schöier, F. L., Jørgensen, J. K., van Dishoeck, E. F., & Blake, G. A. 2002, A&A, 390, 1001
Schöier, F. L., van der Tak, F. F. S., van Dishoeck, E. F., & Black, J. H. 2005, A&A, 432, 369
Tafalla, M., Santiago-García, J., Myers, P. C., et al. 2006, A&A, 455, 577
Teague, R., Semenov, D., Guilloteau, S., et al. 2015, A&A, 574, A137
Turner, B. E. 2001, ApJS, 136, 579
van den Ancker, M. E., The, P. S., Tjin A Djie, H. R. E., et al. 1997, A&A, 324, L33
van Dishoeck, E. F., Thi, W.-F., & van Zadelhoff, G.-J. 2003, A&A, 400, L1
van't Hoff, M. L. R., Walsh, C., Kama, M., Facchini, S., & van Dishoeck, E. F. 2017, A&A, 599, A101
Vidal-Madjar, A. 1991, Advances in Space Research, 11, 97
Walmsley, C. M., Flower, D. R., & Pineau des Forêts, G. 2004, A&A, 418, 1035
Watson, W. D. 1976, Reviews of Modern Physics, 48, 513
Willacy, K. 2007, ApJ, 660, 441
Wilson, T. L. 1999, Reports on Progress in Physics, 62, 143
Wisniewski, J. P., Clampin, M., Grady, C. A., et al. 2008, ApJ, 682, 548
Woods, P. M., & Willacy, K. 2009, ApJ, 693, 1360
Wootten, A. 1987, in IAU Symposium, Vol. 120, Astrochemistry, ed. M. S. Vardya & S. P. Tarafdar, 311–318
Yen, H.-W., Koch, P. M., Liu, H. B., et al. 2016, ApJ, 832, 204
Zhang, K., Bergin, E. A., Blake, G. A., et al. 2016, ApJ, 818, L16
Zhang, K., Bergin, E. A., Blake, G. A., Cleeves, L. I., & Schwarz, K. R. 2017, Nature Astronomy, 1, 0130